JOURNAL OF MATERIALS SCIENCE 39 (2004) 6271–6289

Observations and simulations of the low velocity-to-hypervelocity impact crater transition for a range of penetrator densities into thick aluminum targets

O. L. VALERIO-FLORES, L. E. MURR, V. S. HERNANDEZ, S. A. QUINONES
Department of Metallurgical and Materials Engineering, The University of Texas at El Paso, El Paso, TX 79968, USA

Projectile/target impact crater systems involving soda-lime glass/1100 aluminum, ferritic stainless steel/1100 aluminum, and tungsten carbide/1100 aluminum (corresponding to projectile densities of 2.2, 7.89, and ~17 Mg (m^3) at impact velocities ranging from 0.56 to 3.99 km/s were examined by light metallography, SEM, and TEM. Plots of crater depth/crater diameter ratio (p/D_c) versus impact velocity exhibited anomalous humps with p/D_c ranging from 0.8 to 5.5 between 1 and 2 km/s, with hypervelocity threshold or steady-state values of p/D_c (>5 km/s) ranging from 0.4 to 1.0; with the p/D_c values increasing with increasing projectile density in each case. This hump-shaped regime, with exaggerated target penetration depths, appears to occur because projectiles remain relatively intact and unfragmented. The crater geometry begins to change when the projectile fragmentation onset velocity (>2 km/s) is exceeded and fragmentation increases with increasing impact velocity. Computer simulations and validation of these simulations were developed which fairly accurately represented residual crater shapes/geometries and correlated experimentally measured microhardness maps with simulated residual yield stress contour maps. Validated computer simulations allowed representative extrapolations of impact craters well beyond the laboratory where melting and solidification occurred at the crater wall, especially for hypervelocity impact (>5 km/s).

1. Introduction

The low velocity-to-hypervelocity impact crater transition characterized by a so-called "hump" in plots of crater depth-to-crater diameter ratio (p/D_c) versus impact velocity (u_o) was originally observed somewhat simultaneously by Baker [1] and Bernhard and Hörz [2] for steel projectiles impacting aluminum and soda-lime glass projectiles impacting aluminum (1100), respectively. The severity of this anomalous hump was particularly noticeable for the steel projectiles with a density of 7.86 Mg/m^3 in contrast to the aluminum projectiles with a density of 2.7 Mg/m^3, although the steel/aluminum-projectile/target data was not as comprehensive as that for soda-lime glass/aluminum. More recently, Murr *et al.* [3] compared this anomalous impact crater phenomenon for aluminum/copper, soda-lime glass/aluminum, steel/copper, and steel/aluminum; including the data from Baker [1] and Bernhard and Hörz [2]. It was observed that projectile or penetrator density as well as the ratio of projectile density/target density (ρ_p/ρ_t) — or more specifically $(\rho_p/\rho_t)^{1/2}$ — influenced the severity of the p/D_c "hump" between $u_o = 1$ to 2 km/s. Correspondingly, penetration, p (or p/D_c) increased with increasing values of $(\rho_p/\rho_t)^{1/2}$ in the low velocity range: ~2 km/s. At hypervelocity (≥5 km/s) p/D_c values converged to a steady-state value or hypervelocity threshold which also increased with increasing projectile density.

Baker [1] earlier considered hypervelocity to represent impact velocities greater than 3 km/s and identified three different impact crater types: (1) an elongated crater formed at low projectile velocity with the (spherical) projectile embedded essentially intact in the crater bottom, especially for strong (hard) projectiles impacting a weak (soft) target; (2) a more shallow, wide crater characterized by projectile deformation and break-up at some "intermediate" velocity and; (3) an idealized, hemispherical crater at hypervelocity characterized by complete disintegration of the projectile at impact. These general features were observed by Murr *et al.* [3] for a range of projectile/target impact crater systems where crater depth/crater diameter ratios (p/D_c) were plotted against the corresponding projectile (impact) velocities and the anomalous increase in p/D_c was observed at low impact velocities for several projectile/target systems. Valerio *et al.* [4] also presented preliminary data for the current systems which

confirmed the effects of very dense tungsten carbide projectiles impacting aluminum targets.

The need to examine a range of projectile densities has become especially apparent over the past decades as the man-made proportion of orbital debris particles has exceeded the natural debris regime; with dense particles such as gold, tungsten, and other metals contributing to the potential impact projectiles in low-Earth orbit (LEO) [5, 6]. In addition, the shedding of such debris from orbiting satellites and space craft creates a wide range of impact velocities, including very low velocities (<1 km/s) as a consequence of space craft—orbital debris impact differences—in contrast to interplanetary dust and related micrometeoroid projectiles with relatively low densities, impacting at velocities averaging ~20 km/s [6–8]. McBride *et al.* [9] have also recently described the distribution of small-sized debris in LEO utilizing flux data from the NASA Long Duration Exposure Facility (LDEF) [6].

The ability to study impact crater phenomena in the laboratory is limited by the launch capabilities of various guns, including the sabot arrangements for launching very dense projectiles having sufficiently large sizes. Maximum impact velocities seldom exceed 7 km/s even for very light projectiles such as soda-lime glass. In this regard, the residual crater sizes are especially important if associated microstructures and properties are to be investigated and utilized as a basis for validating computer simulations which are necessary in extending the implications of impact crater phenomena beyond the laboratory, and more consistent with the actual environments of LEO and aspects of deeper space.

The present study represents a systematic evaluation of impact crater formation in a soft aluminum target for a wide range of projectile densities and impact velocities. A particular focus of this research was the validation of computer simulations and the extrapolation of impact phenomena to the hypervelocity regime using the validated simulations.

2. Experimental procedures and simulation methods

The target for the impact experiments performed in this study consisted of a 25 cm × 25 cm cast 1100 aluminum plate having a thickness of 3.5 cm. The cast plate had a nominal composition of 99.3 wt% Al, 0.5% Fe, 0.15% Cu, 0.12% S, and 0.04% Ti; and density (ρ_t) of 2.7 Mg/m^3 (g/cm^3). The as-cast microstructure consisted of dendritic precipitates of Fe_xAl in the grain boundaries; with an average grain diameter of 28 μm. The average Vickers microhardness was 30 VHN or 0.3 GPa. Spherical projectiles (3.175 mm in diameter) of soda-lime glass ($\rho_p = 2.2$ Mg/m^3), ferritic (440) stainless steel ($\rho_p = 7.89$ Mg/m^3), and tungsten carbide ($\rho_p \cong 17$ Mg/m^3) were launched against the target from a powder gun having a 7 mm diameter bore barrel for projectile velocities, u_o, below 3 km/s; and a 5 mm bore, light-gas gun was employed for impact velocities at and above 3 km/s. In the present study, craters were formed at impact velocities u_o of 0.99, 2.00, 2.44, 2.71, 3.11, and 3.99 km/s for the soda-lime glass (SLG) projectiles; 1.08, 2.03, 2.57, and 3.15 km/s for the stainless steel (SS) projectiles, and 0.49, 0.56, 1.0, 1.5, and 1.98 km/s for the tungsten carbide (WC) projectiles. The WC projectiles at velocities of 1.5 and 1.98 km/s were impacted into the thickness face of the target plate to insure against perforation. Actual experiments were carried out in the Experimental Impact Laboratory, SN4, NASA-Johnson Space Center, Houston, TX, USA. The projectile velocities were determined by the occultation of laser beams (2 to 4 stations) and two independent impact-flash detectors, one located at the sabot stripper, and another located at the target positioned approximately 8 m down range from the gun muzzle.

The experimental impact craters were removed from the aluminum target plate in blocks using a plate cutter with a cooling system. Removed blocks containing a crater were photographed and then sectioned with a Buehler high-speed precision diamond saw to produce one exact half section which allowed the crater geometry (crater depth, p, and crater diameter, D_c) to be accurately measured and photographed after grinding and polishing. The polished half sections were also etched using a Keller's reagent composed of 0.15 L H_2O, 3 mL HNO_3, 6 mL HCl, and 6 mL HF cooled to 0°C using an ice bath. A Reichart MEF4M optical metallograph was then used to photograph each crater microstructure. Craters were also observed in a scanning electron microscope (SEM).

Vickers microhardness measurements were made on the polished and etched crater half sections using a digital Shimadzu HMV-2000 microhardness tester. A diamond indenter with a 50 gf (0.5 N) load was employed for indentation times of 10 s. Microhardness measurements were initially made along the impact axis from the crater base as nominal zero, and extending into the target. Additional microhardness profiles were obtained along different directions assuming the crater wall bottom at the intersection of the impact axis with the crater bottom as the zero point of reference (x, $y = 0, 0$) to produce characteristic microhardness maps extending from the crater wall into the target as originally described by Quinones and Murr [10]. These experimentally constructed, residual microhardness maps for each crater were then compared with computer simulated, residual yield stress maps by considering that for common metals such as aluminum the Vickers microhardness values are nominally 3 times the corresponding yield stress (VHN $\cong 3\sigma_y$); where 1 VHN (Vickers Hardness Number) = 1 Kbar = 0.1 GPa.

Finally, three millimeter discs were punched from thin (~200 μm) ground slices cut from the crater half sections as well as sections cut parallel to the crater walls, at various locations at increasing distances from the crater bottom and walls in order to examine the corresponding microstructures in the transmission electron microscope (TEM). The 3 mm discs were electropolished to electron transparency in a Struers-Tenupol 3, dual-jet electropolisher using a solution of 1.2 L methanol and 0.3 L HNO_3 at −20°C. A Hitachi H-8000 analytical TEM was operated at 200 kV, employing a

TABLE I Input parameters for WC, SS, and SLG projectiles used in the simulations

Parameter	WC	SS	SLG
Equation of state	Shock	Linear	Polynomial
Strength model	Johnson-Cook	Johnson Cook	Johnson-Holmquist
Reference density (g/cm^3)	17	7.89	2.2
Bulk modulus (Mbar)	–	1.64	–
Reference temperature (K)	3.00E+02	3.00E+02	3.00E+02
Gruneisen coefficient	1.54	–	–
Specific heat (Terg/gK)	1.34E−06	4.52E−06	8.80E−06
Shear modulus (Mbar)	1.60	8.00E−01	3.00E−01
Yield stress (Mbar)	(1.5) 6.00E−02	7.40E−03	–
Hardening constant (Mbar)	(1.8) 6.00E−03	3.80E−03	–
Hardening exponent	(1.2) 7.00E−01	3.20E−01	–
Strain rate constant	1.60E−02	6.00E−02	–
Thermal softening exponent	(1.0) 5.00	5.50E−01	–
Melting temperature (K)	1723	1811	–
Hydro tensile limit (Mbar)	−9.00E−02	–	−2.00E−03
Intact strength constant A			9.30E−01
Intact strength exponent N			7.70E−01
Strain rate constant C			3.00E−03
Fract. strength constant B			8.80E−02
Fract. strength exponent M			3.50E−01
Max.fract. strength ratio			5.00E−01
Damage constant $D1$			5.30E−02
Damage exponent $D2$			8.50E−01
Hugoniot elastic limit (Mbar)			5.95E−02
Crack softening (GJ/m^2)			4.00E−03
$A1$ (Mbar)			4.54E−01
$A2$ (Mbar)			−1.38
$A3$ (Mbar)			2.90
Failure model	Hydro	None	Johnson-Holmquist
Erosion	None	Inst. Geometric Strain 1.5	None

Note numbers in parenthesis are experimental values which were modified to produce valid simulations.
Erosion strains have no physical measure and the erosion algorithm is simply a numerical technique for avoiding grid tangling in Lagrangian processor calculations.
Note 1 Mbar = 10^2 GPa.

goniometer-tilt stage in observing the thinned specimen regions.

AUTODYN-2D (version 3.0) hydrocode software was used in the impact crater simulations to be reported herein. This is an interactive, integrated hydrocode available on a PC-compatible disk [11, 12]. Lagrange, Euler, Arbitrary Lagrange Euler (ALE) and Shell processors are available and can be coupled if desired. Both Lagrange and Euler processors were used in this study and simulations were carried out for the series of impacts until the geometry of each simulated crater essentially matched the geometry of the actual crater. The software was installed on a Dell Optiplex PC with a 1.7 GHz Pentium 4 chip, and a 1.44 MB floppy drive/256 MB Non-ECC SDRAM memory. Computations often took less than 0.5 h and outputs were printed on an HP Deskjet 960 C printer or similar printers depending upon the resolution and color acuity desired. An Eulerian processor was chosen to model the impacts achieved by SLG ($\rho_p = 2.2$ Mg/m^3) projectiles into the 1100 aluminum target ($\rho = 2.7$ Mg/m^3) at velocities ranging from 0.99 to 3.99 km/s. Lagrange and Euler processors were used to stimulate the harder SS ($\rho_p = 7.89$ Mg/m^3) projectiles for velocities from 1.08 to 3.15 km/s impacted on the same target. However, the Euler processor showed more accurate results for large materials distortion. WC projectiles ($\rho_p \cong 17$ Mg/m^3) were treated using the Euler processor from 0.49 to 1.98 km/s.

The AUTODYN 3.0 hydrocode can produce numerous plots based on pressure, temperature, stress, strain, strain rate, etc. in addition to material grid plots. In this study we were particularly interested in producing crater half sections with corresponding residual yield stress maps so that valid crater geometries could be achieved along with correlations with the experimental, residual microhardness maps developed for each crater half section. The input parameters into AUTODYN 3.0 for the projectiles and the 1100 aluminum target systems explored in this study was set up as noted above for processors specific to each crater simulation. A corresponding matrix of the important input variables for the projectiles and target is provided in Tables I and II respectively. Especially notable in Tables I and II is the diversity of units in contrast to S.I. units which are embedded in standard data libraries for AUTODYN. As noted in Tables I and II the equations of state were varied with the projectile/target system.

The Johnson-Cook constitutive relationship or strength model was applied to the SS and WC projectiles as well as the 1100 Al target, while von Mises and Johnson–Holmquist strength models were applied to the SLG projectiles. The Johnson-Cook [13] constitutive relationship has the general form:

$$\sigma = (\sigma_o + B\varepsilon^n)(1 + C(\ln\dot{\varepsilon}/\dot{\varepsilon}_o))(1 - (T^*)^m) \quad (1)$$

where σ_o, B, C, n, and m are experimentally determined material constants, ε is the strain, $\dot{\varepsilon}$ is the strain

TABLE II Input parameters for 1100 soft aluminum target employed in the simulations for the different systems (WC/1100 Al, SS/1100 Al, and SLG/1100 Al)

Parameter	WC/1100 Al	SS/1100 Al	SLG/1100 Al
Equation of state	Linear	Linear	Shock
Strength model	Johnson-Cook	Johnson Cook	Johnson-Holmquist
Reference density (g/cm^3)	2.7	2.7	2.7
Bulk modulus (Mbar)	7.00E−01	7.00E−01	7.00E−01
Reference temperature (K)	3.00E−02	3.00E−02	3.00E+02
Specific heat (Terg/gK)	8.84E−06	8.84E−06	8.84E−06
Shear modulus (Mbar)	2.71E−01	2.71E−01	2.71E−01
Yield stress (Mbar)	(6.9) 1.00E−03	9.60E−04	1.00E−03
Hardening constant (Mbar)	(5.8) 4.00E−04	6.60E−04	4.20E−04
Hardening exponent	4.80E−01	5.50E−01	4.30E−01
Strain rate constant	(×4) 4.00E−03	1.20E−02	1.10E−02
Thermal softening exponent	1.12	(1.13) 1.17	1.12
Melting temperature (K)	923	923	923
Hydro tensile limit (Mbar)	−4.00E−3	–	−3.00E−3
Gruneisen coefficient	–	–	2.00
C1 (cm/us)	–	–	5.386E−01
S1 (cm/us)	–	–	1.338
Failure model	Hydro	Johnson - Cook	Hydro
Erosion	None	1.5	None

See notes for Table I.

rate, $\dot{\varepsilon}_o$ is a reference strain rate (usually equal to unity), and

$$T^* = (T - T_r)/(T_m - T_r), \tag{2}$$

where T_m is the melting temperature, T_r is a reference temperature at which σ_r is measured, and T is the temperature at which σ is calculated:

$$\sigma = \sigma_r[1 - (T - T_r)/(T_m - T_r)^m] \tag{3}$$

Correspondingly, the von Mises equation is expressed by

$$\sigma_y = [((S_1-S_2)^2+(S_2-S_3)^2+(S_3-S_1)^2)/2]^{1/2} \tag{4}$$

where σ_y is the yield strength (or stress) and S_1, S_2, and S_3 are the deviatoric stress components. The Johnson-Holmquist strength model is particularly applicable to brittle, strong materials such as glass and other ceramics [14] and gives the yield stress as a function of pressure. The equation is a simple polynomial.

The instantaneous Hugoniot shock pressure at impact in the target was calculated for each impact crater from:

$$P_S = \rho_t(C_t + S_t U_{pm})U_{pm} \tag{5}$$

where ρ_t is the aluminum target density (2.7 Mg/m^3), C_t is the bulk sound velocity in the target, S_t is a target material constant related to the Grüneisen parameter, and U_{pm} is the modified projectile velocity in the compressed region after impact and given by [15]:

$$U_{pm} = [-(\rho_t C_t + \rho_p C_p + 2\rho_p S_p u_o) \pm (\Delta)^{1/2}]/2(\rho_t S_t - \rho_p S_p), \tag{6}$$

where

$$\Delta = (\rho_t C_t + \rho_p C_p + 2\rho_p S_p u_o)^2 + 4(-\rho_p)(\rho_t S_t - \rho_p S_p)\left(C_p u_o + S_p u_o^2\right) \tag{7}$$

and ρ_t and ρ_p are the target and projectile densities, C_p and S_p are the corresponding bulk sound velocity and Grüneisen-related material parameters respectively for the projectile, and u_o is the projectile velocity at impact.

In the hydrodynamic regime during crater formation, the so-called steady-state pressure was calculated from the Bernoulli equation:

$$P_B = \left[\rho_p\rho_t\Big/\left(\rho_p^{1/2} + \rho_t^{1/2}\right)^2\right]u_o^2/2 \tag{8}$$

where ρ_p and ρ_t are the projectile and target densities and u_o is the impact velocity. The Bernoulli pressure is sometimes associated with the so-called steady-state pressure at the crater bottom when the crater is actually formed, and represents an attenuation of the Hugoniot pressure. Consequently it is considerably less than the instantaneous shock pressure.

3. Results and discussion

Figs 1 to 3 compare low and high impact velocity examples for the three experimental impact crater systems: SLG/Al, SS/Al, and WC/Al, respectively. In the reverse order, the crater cross-section views in Figs 1–3 show the characteristic crater shapes described by Baker [1] as well as the evolution of these shapes within individual systems as a function of increasing impact velocity, u_o, as well as the pronounced effect of projectile density in progressing from Figs 1 to 3, characterized by $\rho_p = 2.2$, 7.89, and 17 Mg/m^3 respectively. The crater shape evolution with increasing projectile velocity and the onset and evolution of projectile fragmentation and eventual disintegration at the highest experimental impact velocity for SLG at 3.99 km/s in Fig. 1d is also highlighted on comparing Fig. 4a and b and Fig. 5, which are progressively tied to the crater shape evolution in Figs 1 to 3, respectively. Fig. 1e also illustrates, schematically, the convention for measuring crater geometries: penetration depth, p, and crater diameter, D_c.

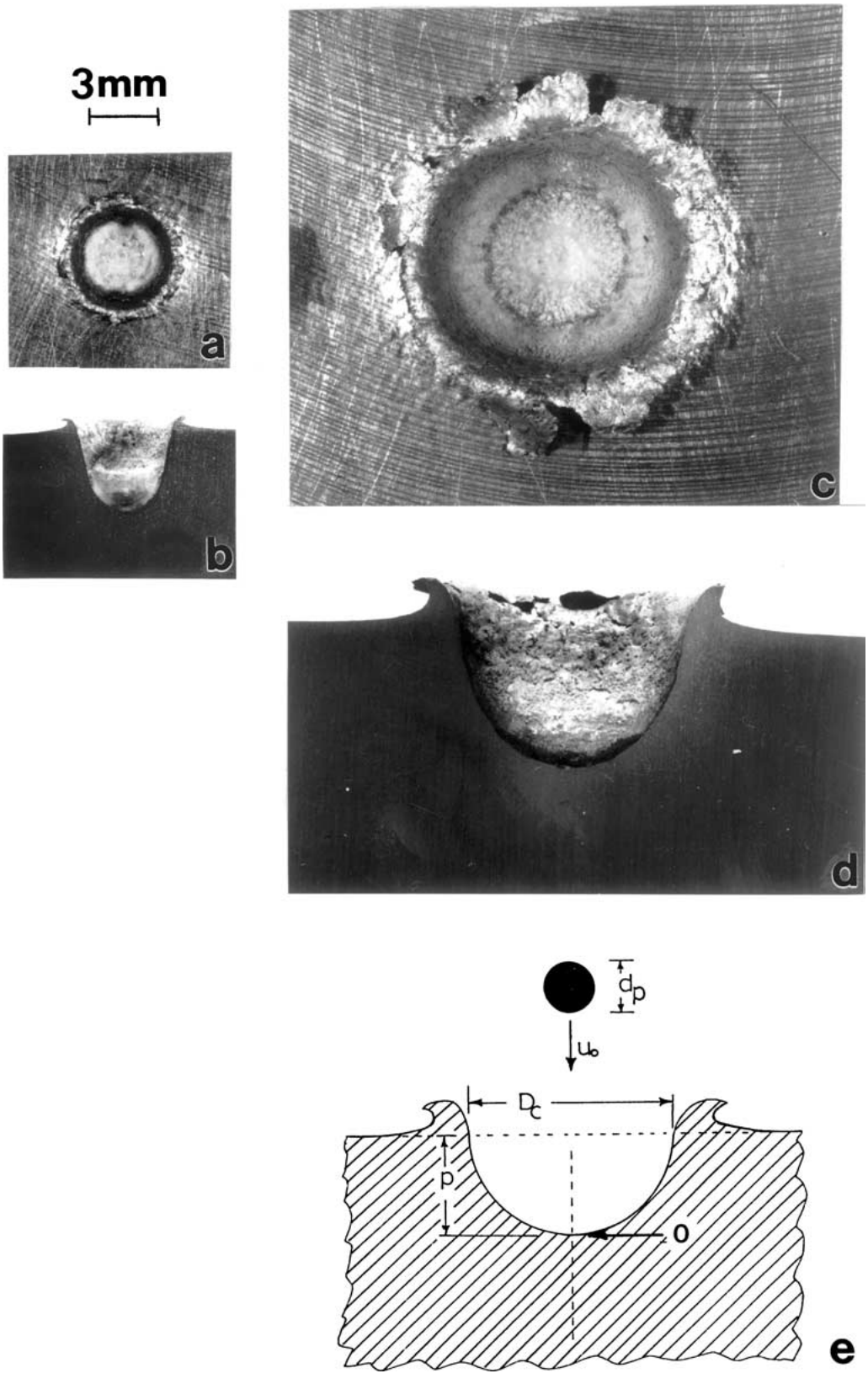

Figure 1 Soda-lime glass projectile impact craters in 1100 aluminum. (a) Top and (b) cross-section views for $u_o = 0.99$ km/s. (c) Top and (d) cross-section views for $u_o = 3.99$ km/s. The magnification for all figures is shown above (a). (e) Schematic cross-section view showing crater geometry conventions. d_p is the projectile diameter; constant at 3.175 mm in this study. u_o is the impact velocity, p is the crater depth and D_c is the crater diameter. The impact axis is shown dotted as an extension of the u_o arrow. The crater bottom is referenced to 0 along the impact axis.

Figs 1b and 4a illustrate fragmented and mostly intact but distorted projectile material within the crater, while Figs 2b and 3d as well as Figs 3b and 5b, show projectiles in relatively undistorted or partially distorted conditions in the impact craters. Figs 1 to 3 also show increasing penetration or crater elongation with increasing projectile density which is especially prominent for the 1.98 km/s WC projectile-developed crater shown in Fig 3d. In this regard Figs 1 to 3 illustrate increasing and exaggerated deviation from the hemispherical-type

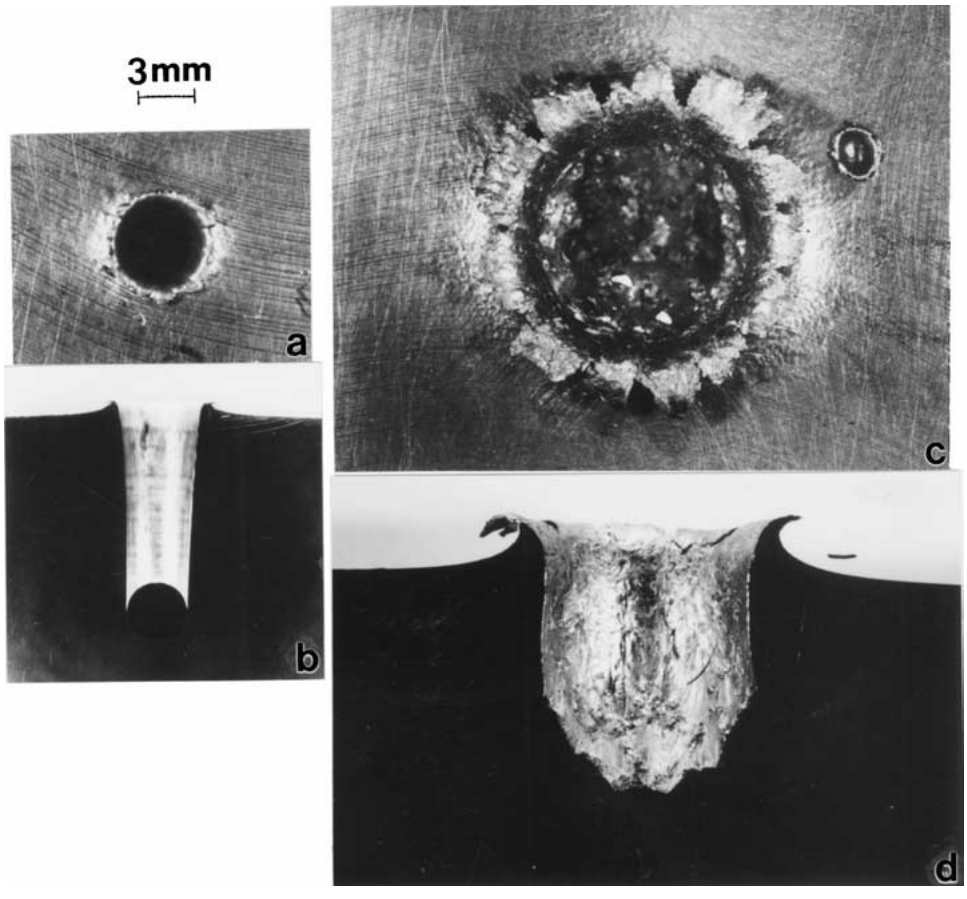

Figure 2 Stainless steel projectile impact craters in 1100 aluminum. (a) Top and (b) cross-section views for $u_o = 1.08$ km/s. (c) Top and (d) cross-section views for $u_o = 3.15$ km/s. Magnification for all figures is shown above (a).

crater which is characteristic of hypervelocity impact: $\geq$5 km/s. Figs 1 to 3 also illustrate the evolution of the crater rim with increasing impact velocity where there is a proportionate scaling of the crater rim width with the difference in impact velocity.

Fig. 6 compares the residual Vickers microhardness profiles from the bottom of the craters and along the impact axis (shown dotted in Fig. 1e) into the target. The maximum hardness values very close to the crater walls nearly double for each impact crater system in Fig. 6, while the general shape of the hardness decline into the target from the crater bottom is essentially unchanged; decreasing exponentially with distance from the crater bottom. It can be noted that the extent of target hardening appears to be less for the WC/Al system in Fig. 6c but if the 2 km/s impact crater for the SLG/Al system in Fig. 6a is compared with the 1.98 km/s impact crater for the WC/Al system in Fig. 6c, the convergence to the base target hardness of $\sim$30 VHN (or 0.3 GPa) is essentially the same, reaching the base hardness at roughly 7.5 mm from the crater base (at 0 in Fig. 1e).

While there is no apparent softening at the crater wall represented by the microhardness profiles in Fig. 6, this is due to the fact that the base (target) material was especially soft and the hardened target next to the crater was also not particularly hard. This prevented the indenter from approaching the crater wall and accurately representing the softening which only extended roughly 0.2 mm at most into the target. Some softening is noted for the SLG/Al system in Fig. 6a especially at 2 km/s but this is the only direct experimental indication of softening at the crater wall.

Fig. 7 illustrates a few typical examples of the microstructures which were characteristic of the deformed zones surrounding the crater, in the target, and extending from the crater base, as illustrated in the corresponding microhardness profiles shown in Fig. 6. Fig. 7a shows a mostly recrystallized region between the crater side wall in Fig. 2d and roughly 1 mm into the target while Fig. 7b shows heavily dislocated recovery microstructures just beyond this zone at $\sim$1 mm from the crater wall. Fig. 7c shows microbands coincident with {111} plane traces intermixed with the recovery-type dislocation microstructures shown in Fig. 7b roughly 3 mm from the crater wall in Fig. 2d. These microstructures essentially characterize the microhardness trends as indicated by the arrows in Fig. 6b specifically, and indeed in the associated microhardness profiles for the SLG/Al and WC/Al systems shown in Fig. 6a and c, respectively. Microstructures similar to Fig. 7a to c have been observed in the SLG/Al system by TEM analysis in the earlier work by Murr *et al.* [3], and dynamically recrystallized grain structures were observed for an impact crater in aluminum 1100 corresponding to a SLG projectile at 6.13 km/s. Fig. 7d shows the target (base) microstructure to consist of dislocation cells having a mean diameter of roughly 1.3 μm. These microstructures are observed in the targets at 20 mm or more from the crater wall. It is instructive to note the variations

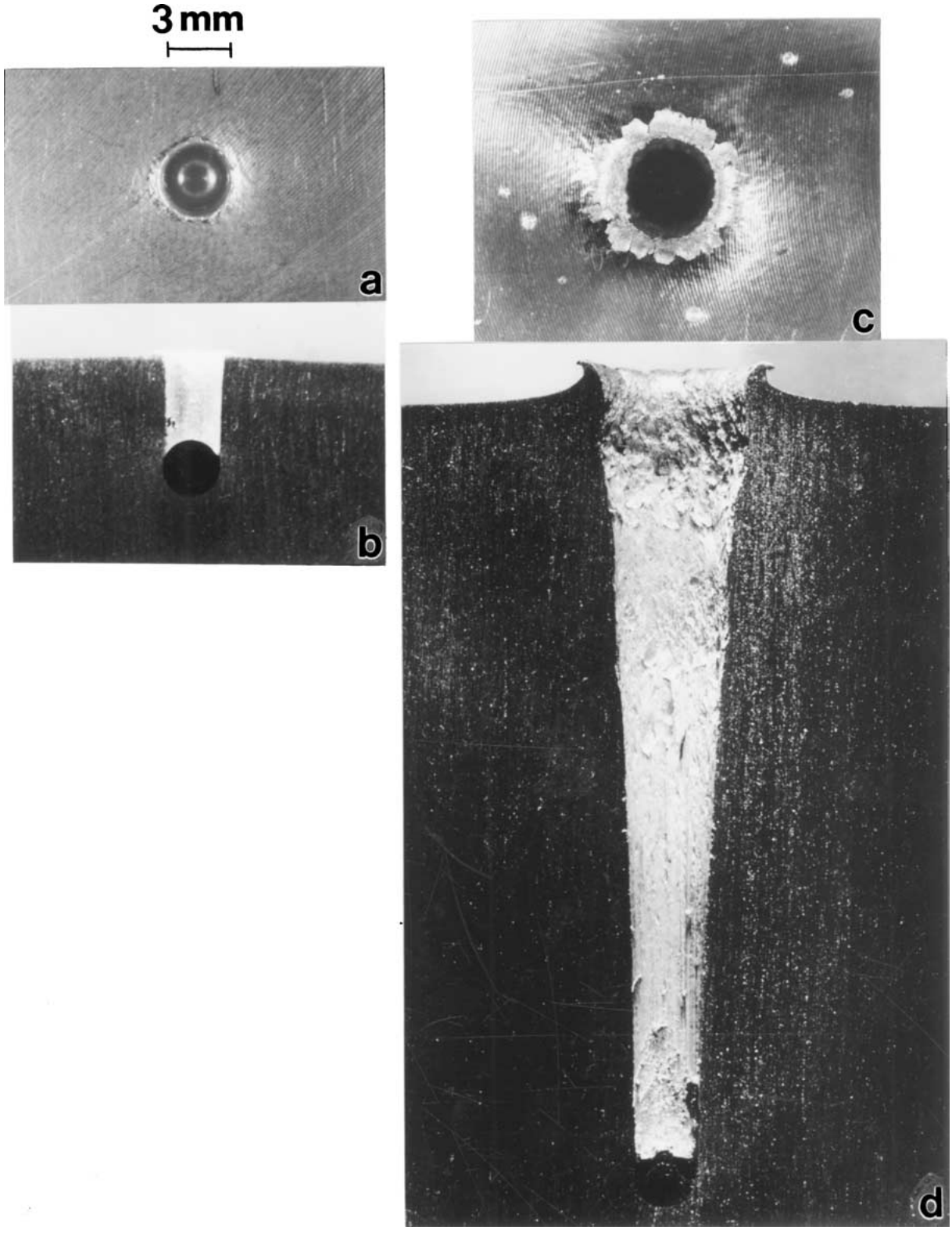

Figure 3 Tungsten carbide projectile impact craters in 1100 aluminum. (a) Top and (b) cross-section views for $u_o = 0.56$ km/s. (c) Top and (d) cross-section views for $u_o = 1.98$ km/s. Magnification for all figures is shown above (a).

in crater-related microstructures shown in Fig. 7a–c in contrast to the base dislocation cell structure shown in Fig. 7d. Note also that the recovery and recrystallization structures shown in Fig. 7a and b as well as the intermixed microbands in Fig. 7c have dimensions roughly half the dislocation cell dimensions in Fig. 7d. It was also noted that between Fig. 7c and d, the microstructures in the target were characterized by dislocation cells which increased in size from roughly 0.5 μm in average diameter to the base target dislocation cell size of $\sim$1.3 μm as shown in Fig. 7d. These features were generally observed for other crater systems and are reflected in the corresponding microhardness data profiles shown in Fig. 6.

The microhardness profiles and associated residual target microstructures represented in Figs 6 and 7 are more appropriately represented in the crater cross-sections illustrated in Figs 1 to 3 by microhardness

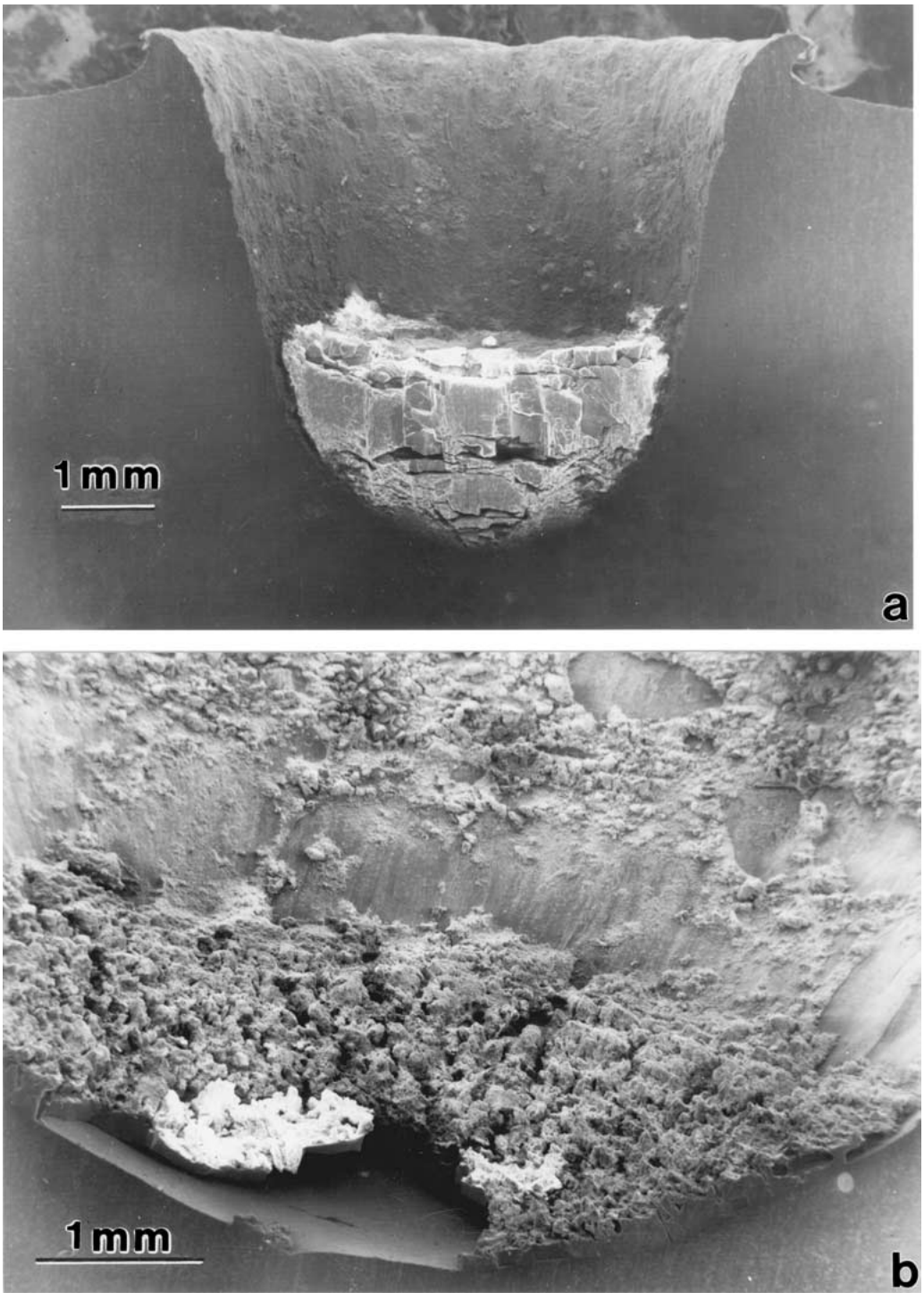

Figure 4 Magnified views of the soda-lime glass impact craters in Fig. 1 showing residual projectile fragments in the crater: (a) $u_o = 0.99$ km/s. and (b) $u_o = 3.99$ km/s.

mappings and simulated residual yield stress maps. Fig. 8 compares these features for the SLG/Al system, as illustrated in Fig. 1, for impact craters corresponding to 0.99 and 3.99 km/s. Fig. 8 illustrates simulated yield stress and experimental microhardness maps for the crater half sections on the same scale (magnification) where the relative zone sizes are observed to be very similar especially at the crater base. Note the projectile remanent in Fig. 8a in comparison to the actual crater cross-section views in Figs 1a and 4a. It is also interesting to observe a simulated soft (dynamically recrystallized) zone for the simulated crater at 3.99 km/s in Fig. 8c. The simulated crater geometries (p, D_c, and p/D_c) in Fig. 8a and c closely matched the experimental crater geometries and together with the close match between residual yield stress maps (or zones) and microhardness (with equivalent yield stress range noted) maps, provided sufficient validation over the range of experimental impact velocities, to allow relatively confident extrapolations into the hypervelocity regime. These extrapolations are illustrated in the computer simulations at 5 and 10 km/s impact velocity for the SLG/Al system as shown reproduced in Fig. 9. Fig. 9 illustrates a somewhat more pronounced dynamic recrystallization zone (DRX) especially at 10 km/s (Fig. 9b). Note also in Fig. 9b that the crater is approaching

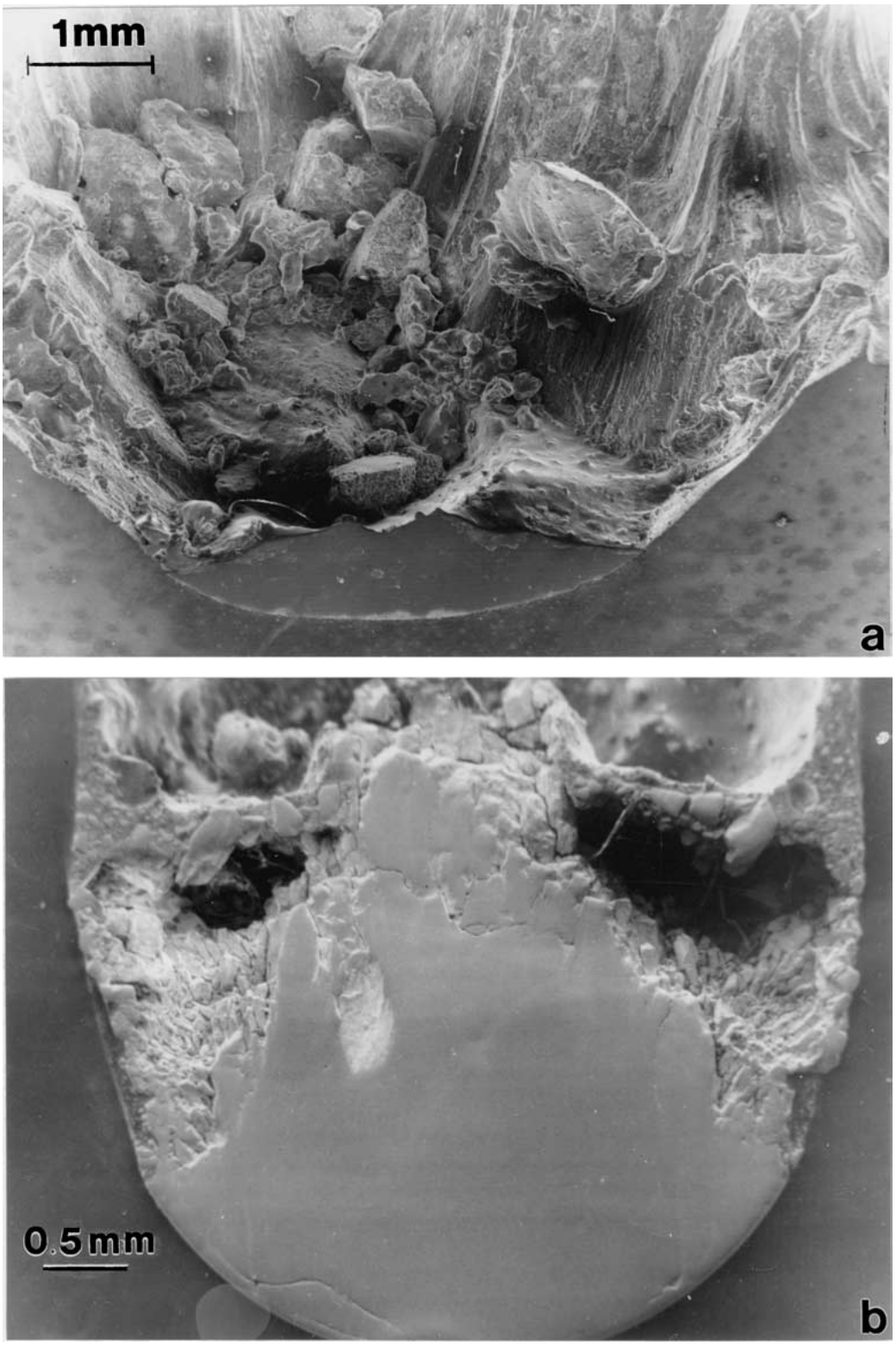

Figure 5 Magnified views of stainless steel and tungsten carbide impact craters in Figs. 2b and 3b with projectiles. (a) Stainless steel crater; $u_o = 3.15$ km/s. (b) Tungsten carbide crater; $u_o = 1.98$ km/s. After Ref. 14.

an ideal, hypervelocity hemispherical-like shape, but $p/D_c = 0.63$ in contrast to an ideal hemisphere where $p/D_c = 0.5$.

Table III summarizes the impact crater geometry data for the SLG/Al system along with the corresponding data for the SS/Al and WC/Al systems. The summary in Table III also includes calculated Hugoniot shock (P_S) and Bernoulli (P_B) pressures for comparison. It can be noted on perusing the calculated pressures that at 10 km/s, the instantaneous and steady-state pressures vary from 150 to 30 GPa for SLG/Al (Table III). Temperatures produced in the cratering process are pressure dependent and consist of two components: the adiabatic temperature rise at the shock front and the residual temperature rise associated with the formed crater and residual heating of the target. For aluminum, adiabatic temperatures in the shock front will equal the melting temperature (~933 K) between roughly

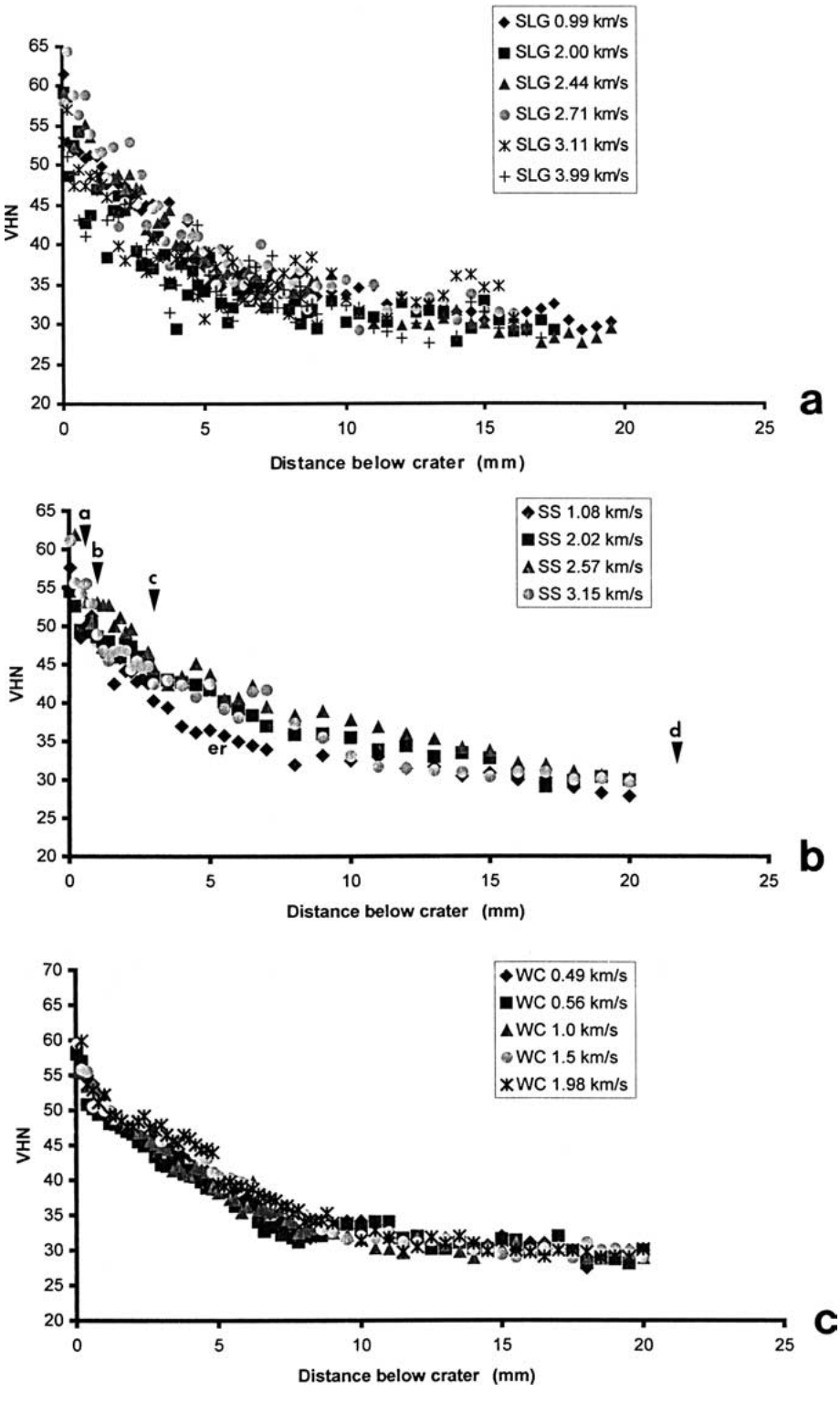

Figure 6 Crater axial microhardness versus distance from the crater bottom (at 0 in Fig. 1e) for the three experimental systems. (a) Soda-lime glass (SLG) projectiles at velocities shown. (b) Stainless steel (SS) projectiles at velocities shown. (c) Tungsten carbide (WC) projectiles at velocities shown. The arrows in (b) correspond to specific microstructures illustrated in Fig. 7a, b, c, and d respectively for $u_o = 3.15$ km/s.

40–50 GPa [15–17]. However, the residual temperature rise will approach the melting temperature only when the Hugoniot or instantaneous pressure exceeds about 90 GPa. It is therefore possible that softening exhibited in the simulation of a 10 km/s SLG/Al crater as shown in Fig. 9b is not DRX alone but rather a mixture of surface melt and an underlying recrystallized (DRX) zone.

Fig. 10 shows, in correspondence with Fig. 2, the simulated yield stress maps and the experimental microhardness maps for SS/Al craters at 1.08 and 3.15 km/s. As noted in Table III, the corresponding impact crater geometries are again very close and there is qualitative agreement between the simulated yield stress maps and the experimentally measured microhardness maps. Fig. 11 shows an extrapolated, simulated SS/Al impact crater for a projectile velocity of 5 km/s. Note the thin but discontinuous soft zone at the crater wall in Fig. 11. Note also from the calculated pressures in Table III that the instantaneous and steady-state pressures vary from ~90 to ~13 GPa.

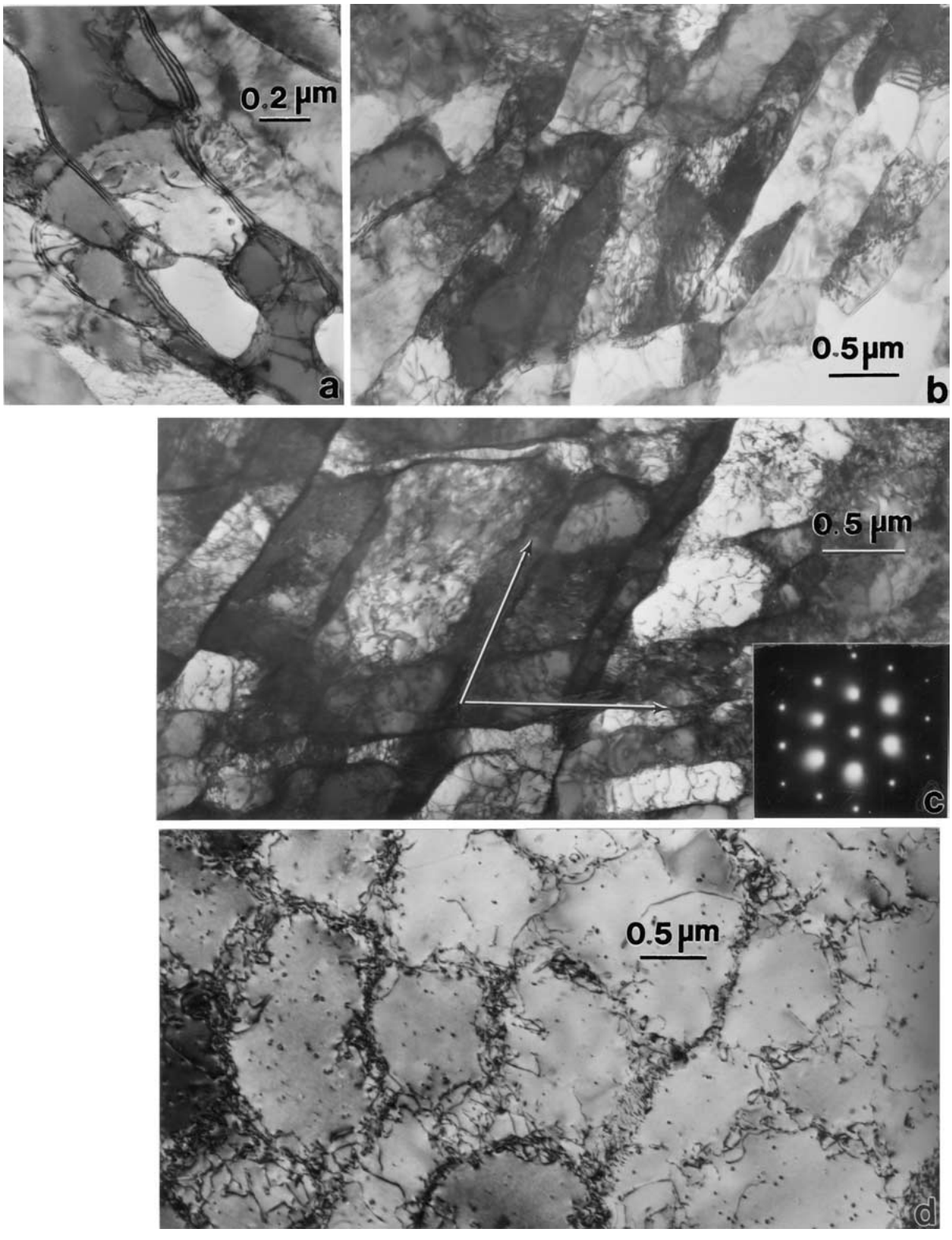

Figure 7 TEM bright-field images for microstructures associated with 3.15 km/s stainless steel impact craters in 1100 aluminum. (a) ≤1 mm from the crater side wall. (b) ∼1 mm from the crater side wall. (c) ∼3 mm from the crater side wall. Microbands concident with the {111} planes are indicated by the ⟨112⟩ trace directions shown. The selected-area electron diffraction pattern insert shows a symmetrical (110) surface orientation. (d) Target base microstructure.

Figs 12 and 13 complete the simulation-experimental impact crater comparisons and extrapolations for the WC/Al system. Fig. 12 corresponds to the impact craters represented in the cross-section views in Fig. 3 for WC projectile velocities of 0.56 km/s and 1.98 km/s. The relatively intact, remanent projectiles are simulated within the craters and the simulated crater view, including the residual yield stress map, illustrates a very thin soft zone or DRX zone at the crater wall (Fig. 12c). In addition, the simulated impact crater cross-section in Fig. 12c provides a slightly more prominent view of a peculiar penetration effect characterized by what appears to be three zones, each with a decreasing crater diameter. This feature is also especially prominent in the experimental cross-section shown in Fig. 3d where there appears to be an initial, regular crater forming

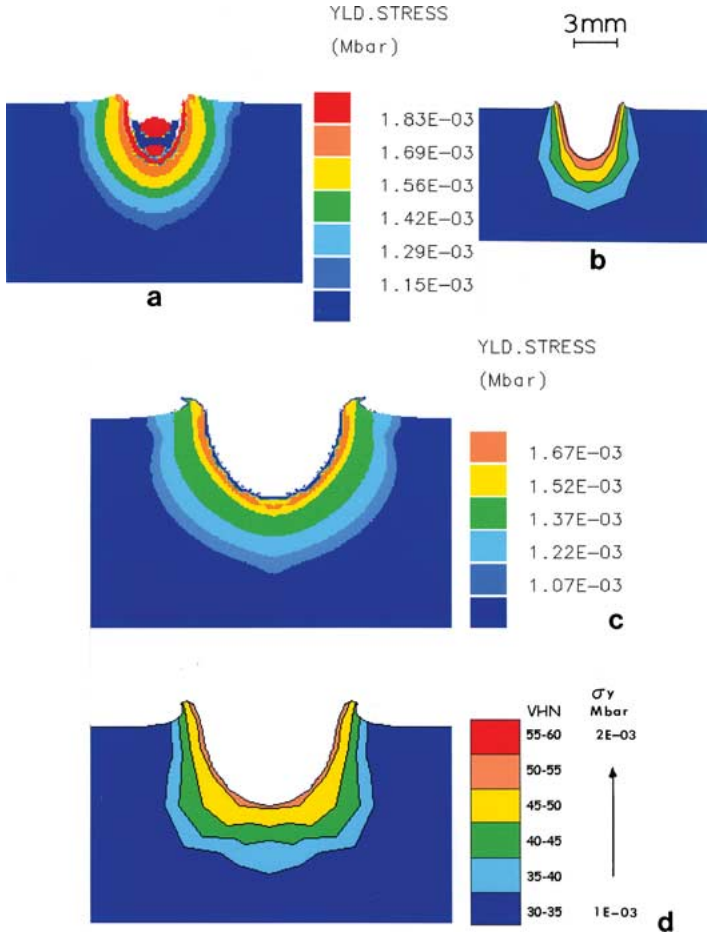

Figure 8 Comparison of computer simulated and experimental impact crater half-sections for the SLG/Al system. (a) Simulated impact crater for $u_o = 0.99$ km/s showing residual yield stress contours and color key. (b) Experimental microhardness (VHN) map for $u_o = 0.99$ km/s (Fig. 1b). Color key is the same as shown in (d). (c) Simulated impact crater for $u_o = 3.99$ km/s showing residual yield stress contours and color key. (d) Experimental microhardness (VHN) map for $u_o = 3.99$ km/s and color key (Fig. 1d). The equivalent yield stress range from 30 VHN (1×10^{-3} Mbar) to 60 VHN (2×10^{-3} Mbar) is indicated by σy (Mbar). Note the scale bar in the upper right corner applies to all figures, and both the x and y-axes.

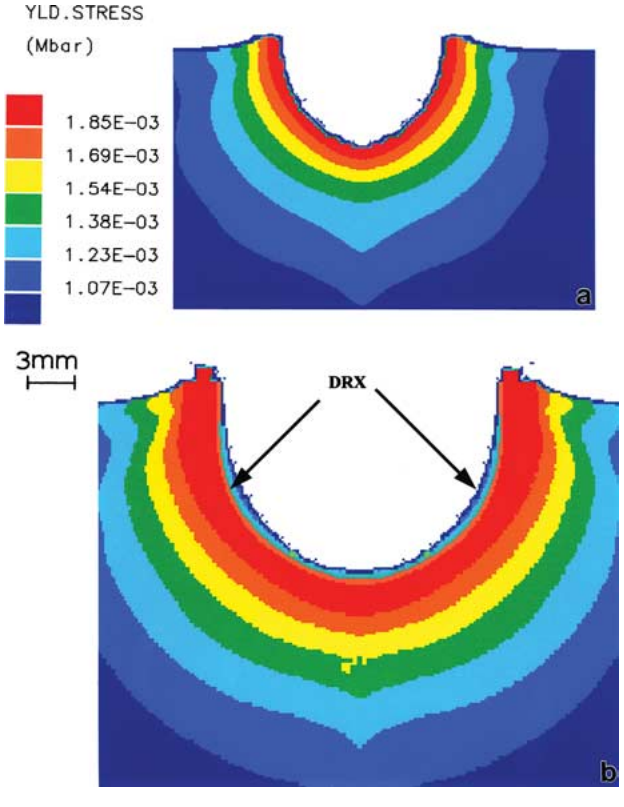

Figure 9 Impact crater simulations for the SLG/Al system at extrapolated hypervelocities showing residual yield stress contours and corresponding color key. (a) $u_o = 5$ km/s. (b) $u_o = 10$ km/s. The color key applies to both (a) and (b). The scale bar shown applies to both figures, and both the x and y-axes. In (b) DRX denotes the dynamically recrystallized zone or soft zone at the crater wall.

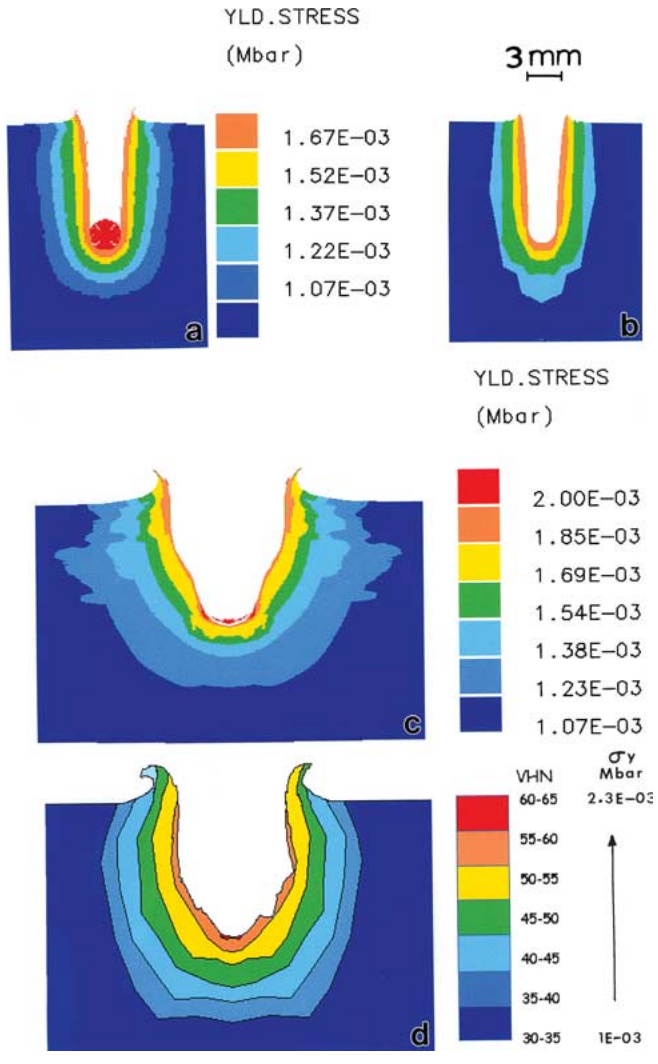

Figure 10 Comparison of computer simulated and experimental impact crater half-sections for the SS/Al system. (a) Simulated impact crater for $u_o = 1.08$ km/s showing residual yield stress contours and color key. (b) Experimental microhardness (VHN) map for $u_o = 1.08$ km/s (Fig. 2b). Color key is the same as shown in (d). (c) Simulated impact crater for $u_o = 3.15$ km/s showing residual yield stress contours and color key. (d) Experimental microhardness (VHN) map for $u_o = 3.15$ km/s and color key (Fig. 2d). The equivalent yield stress range from 30 VHN (1×10^{-3} Mbar) to 65 VHN (2.3×10^{-3} Mbar) is indicated by σy (Mbar). The scale bar in the upper right corner applies to all figures, and both the x and y-axes.

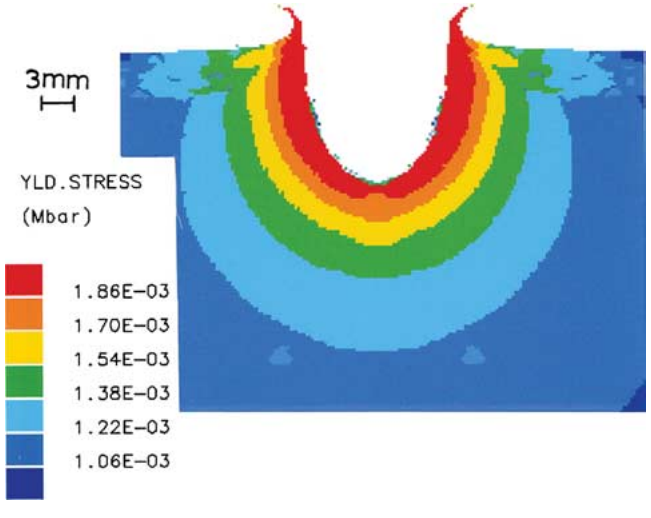

Figure 11 Impact crater simulation for SS/Al system for $u_o = 5$ km/s showing residual yield stress contour corresponding to the color key in Fig. 10c. The scale bar applies to both the x and y-axes.

initially at the target surface, which then transforms into a narrower penetration/crater diameter as the dense projectile continues into the target. Fig. 13 illustrates, somewhat consistent with the other extrapolated simulations, an increasing soft zone at the crater wall as the impacting projectile velocity increases into the hypervelocity regime. As shown in Table III, the calculated pressures at 5 and 10 km/s far exceed the pressures

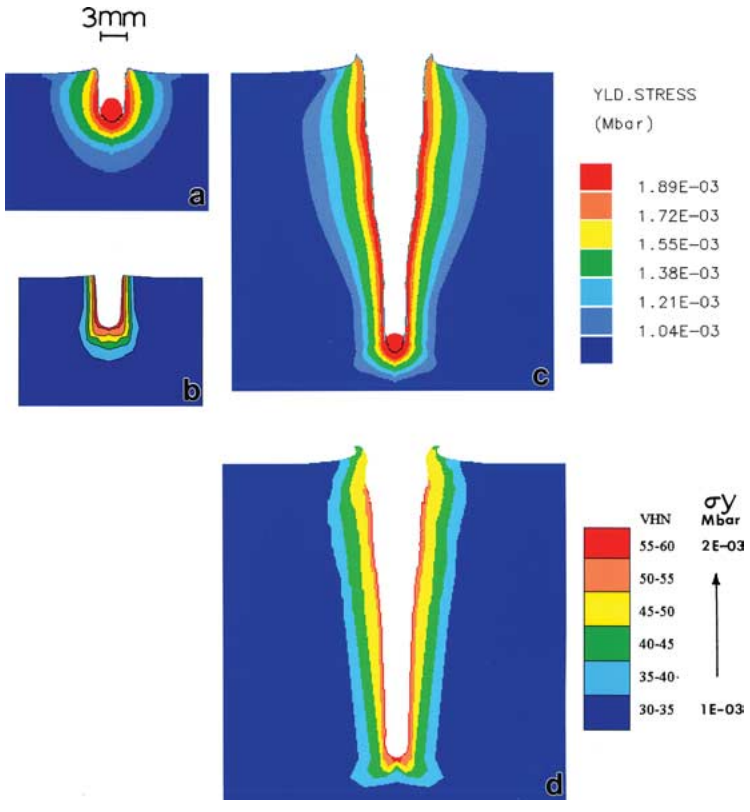

Figure 12 Comparison of computer simulated and experimental impact crater half-sections for the WC/Al system. (a) Simulated impact crater for $u_o = 0.56$ km/s showing residual yield stress contours. The color key is the same as shown in (c). (b) Experimental microhardness (VHN) map for $u_o = 0.56$ km/s (Fig. 3b). Color key is the same as shown in (d). (c) Simulated impact crater for $u_o = 1.98$ km/s showing residual yield stress contours and color key. (d) Experimental microhardness (VHN) map for $u_o = 1.98$ km/s (Fig. 3d) and color key. The equivalent yield stress range from 30 VHN (1×10^{-3} Mbar) to 60 VHN (2×10^{-3} Mbar) is indicated by σy (Mbar). The scale bar in the upper left corner applies to all figures, and both the x and y-axes.

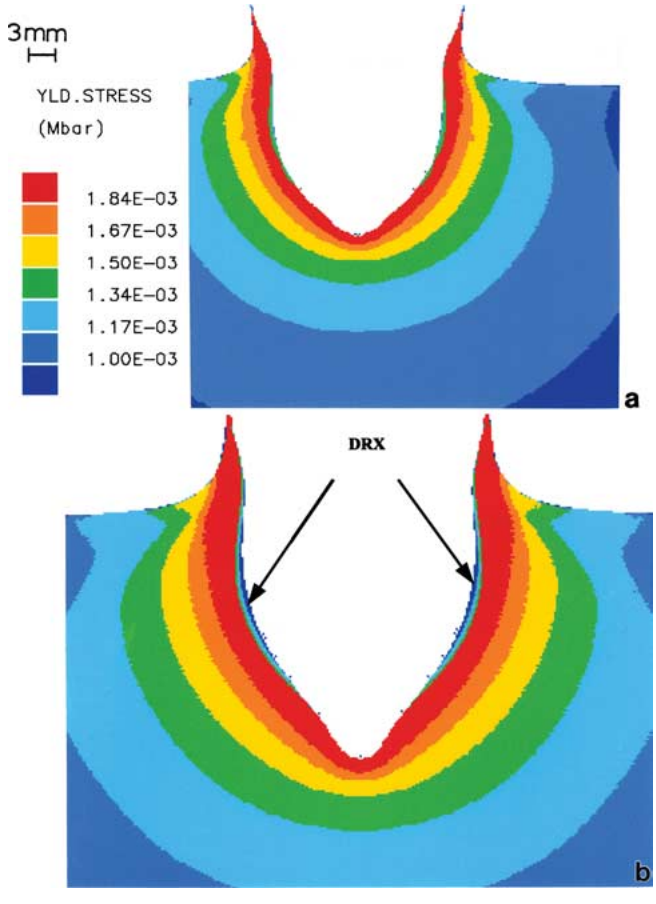

Figure 13 Impact crater simulations for the WC/Al system at extrapolated hypervolocites showing residual yield stress contours and corresponding color key. (a) $u_o = 5$ km/s. (b) $u_o = 10$ km/s. The color key applies to both (a) and (b). The scale bar applies to both figures, and to both the x and y-axes.

TABLE III Projectile/target cratering system data

	Experimental data			Simulated data			Calculated pressures	
Velocity (μ_o) (km/s)	p (mm)	D_c (mm)	p/D_c	p (mm)	D_c (mm)	p/D_c	P_S (GPa)	P_B (GPa)
			Soda-lime glass/1100 aluminum (SLG /Al)					
0.99	3.6	4.1	0.87	3.3	4.3	0.78	6.5	0.3
2.00	5.3	6.9	0.75	5.2	7.0	0.74	15.2	1.2
2.44	5.7	7.8	0.72	5.7	7.9	0.72	19.5	1.8
2.71	6.0	8.2	0.73	6.0	8.3	0.72	22.4	2.2
3.11	7.0	9.8	0.72	7.0	9.9	0.71	27.0	3.0
3.99	6.7	10.5	0.63	6.6	10.4	0.63	37.8	4.8
5.0	–	–	–	7.8	12.5	0.62	52.0	7.6
10.0	–	–	–	11.5	18.1	0.63	150.5	30.4
15.0	–	–	–	13.0	21.3	0.61	294.9	68.4
			Stainless steel/1100 aluminum (SS/Al)					
1.08	11.9	4.0	2.95	11.8	4.1	2.87	13.0	0.6
2.03	11.0	7.0	1.56	11.3	7.5	1.5	27.0	2.0
2.57	12.5	9.7	1.28	12.3	9.7	1.2	37.0	3.5
3.15	13.3	11.9	1.11	13.4	12.0	1.11	48.0	5.0
5.0	–	–	–	15.6	15.3	1.0	89.7	13.4
10.0	–	–	–	16.4	13.7	0.82	254.5	53.7
15.0	–	–	–	11.7	14.7	0.80	494.1	120.7
			Tungsten carbide/1100 aluminum (WC/Al)					
0.49	6.7	3.5	1.9	7.3	4.0	1.8	6.4	0.15
0.56	7.3	3.2	2.2	8.0	4.0	2.0	7.4	0.2
1.0	18.2	4.0	4.5	18.7	4.4	4.3	14.3	0.7
1.5	29.6	5.7	5.2	32.0	5.6	5.1	22.8	1.5
1.98	40.3	7.1	5.6	43.1	8.0	5.4	32.0	2.6
5.0	–	–	–	27.5	24.0	1.1	109.8	16.6
10.0	–	–	–	33.6	33.4	1.0	311.3	66.6
15.0	–	–	–	41.5	38.7	1.0	602.4	149.7

ρ_p (soda-lime glass) = 2.2 Mg/m^3; ρ_p (stainless steel) = 7.89 Mg/m^3.
ρ_p (tungsten carbide) $\cong$ 17 Mg/m^3; ρ_t (1100 aluminum) = 2.7 Mg/m^3.
Note. 1 Mg/m^3 = 1 g/cm^3; 1 GPa = 10^3MPa = 10 kb = 10^{-2} Mb (Mbar).

required for melting along the crater wall, and the soft zone shown in the simulation for a WC/Al crater at 10 km/s in Fig. 13b would likely represent a melt (or solidified) zone, i.e., a zone solidified from the melt rather than a DRX zone.

To examine the impact-melt issue, we revisited a library of images, particularly SEM images, of impact craters in anodized aluminum structures on the NASA Long Duration Exposure Facility (LDEF) [18, 19]. These craters were assumed to be formed primarily by hypervelocity impacts at velocities well above orbital velocity (>8 km/s). Consequently, even assuming very light projectile materials such as interplanetary dust particles or related low-density debris characteristic of the soda-lime glass projectiles utilized in the present study, the corresponding, calculated impact-related pressures would be expected to be in excess of 150 GPa for the instantaneous (Hugoniot shock) pressure, and 30 GPa for the steady-state pressure (Table III). In fact, NASA has considered the average impact velocity on satellites like LDEF to be roughly 20 km/s and this would normally create a melt/solidification zone within craters created in aluminum space structures [6]. This might normally involve the creation of very smooth crater walls or even evidence of gas release through the creation of bubbles or pores in the crater surface. Fig. 14 shows typical SEM images of a crater in an aluminum (anodized 6061) surface on LDEF which illustrate these features and corroborate the foregoing suggestions.

Fig. 15 summarizes the experimental and simulated geometrical crater data (p/D_c versus u_o) tabulated in Table III and illustrated in the image sequences presented in Figs 8 to 13. The corresponding plots show very graphically the correspondence between the experimental and simulated data points related to the geometrical ratio p/D_c, and the general validity of the computer simulations. In addition, the previous results of Baker [1] for steel projectiles impacting aluminum targets also coincides with the current data, along with prior results for the SLG/Al system [3]. It must be cautioned of course that the data plotted in Fig. 15 for the WC projectiles has no experimental values above 2 km/s and as a result the position of the peak, including the simulated data, could actually lie at a higher value of impact velocity. Similarly the stainless steel projectile data has no experimental values below 1 km/s impact velocity and the peak shown for this data could shift to a lower impact velocity. It should be noted in Table III, especially in the context of the p/D_c data summarized in the plots of Fig. 15, that while the computer simulations correspond very closely with the experimental, geometrical ratio data (Fig. 15), there is also very close correspondence of the simulated and experimental values of crater depth, p, and crater diameter, D_c; however deviations tend to become slightly larger as the projectile density increases, and is most notable for the WC projectiles when comparing values of p and D_c for the experimental data and the simulated values. The close correspondence of absolute experimental and

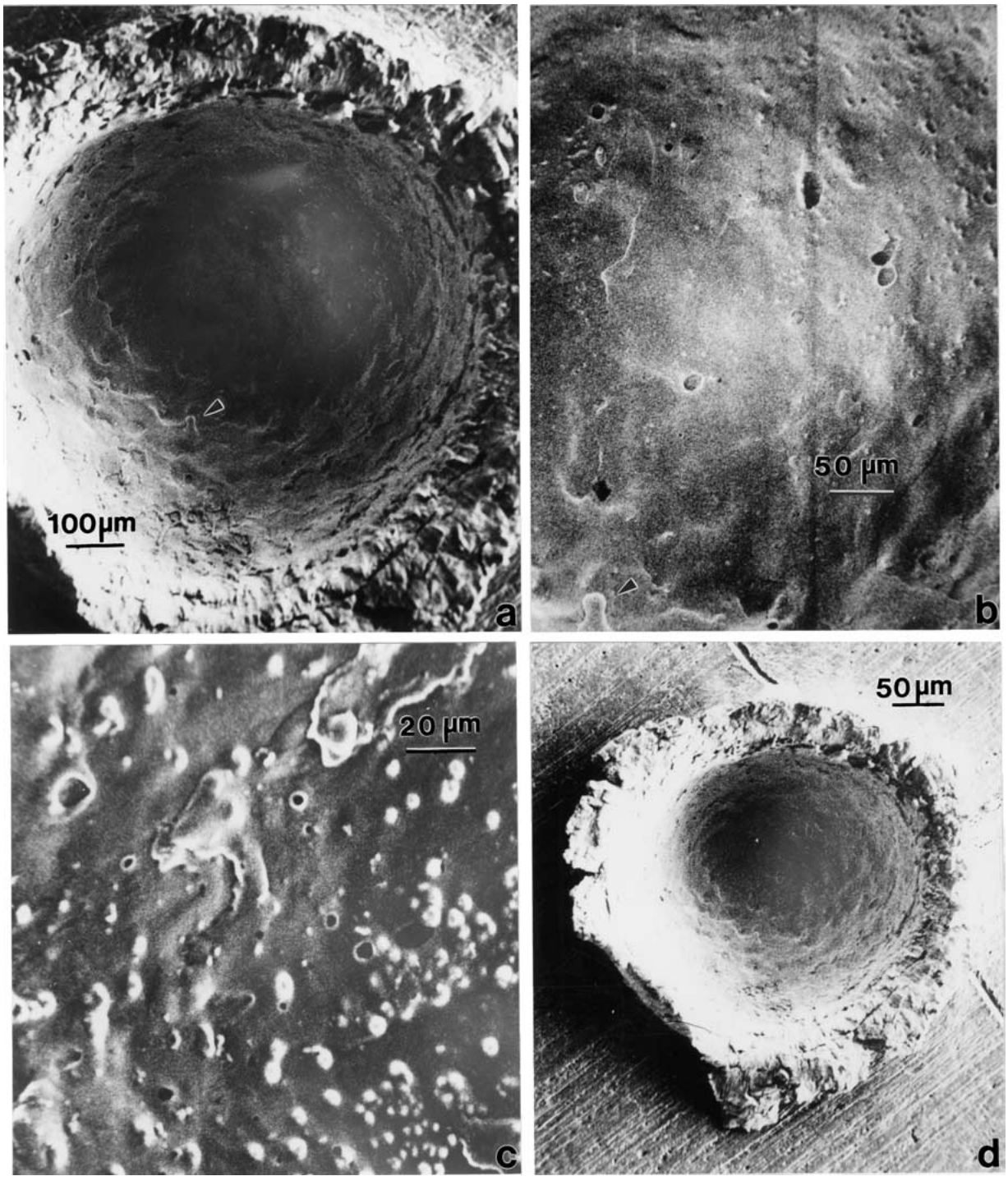

Figure 14 SEM images for examples of impact crater in anodized 6061 aluminum on the NASA-LDEF satellite. (a) Crater view. (b) Magnified view inside crater at reference arrow. (c) Magnified view of upper region in (b) showing gas bubbles. (d) Lower magnification view of the crater.

simulated values for crater diameter, especially within the respective experimental ranges, is more generally illustrated in the plots of D_c versus u_o in Fig. 16. Fig. 16 would also look essentially the same if the crater diameter values were normalized by dividing by the projectile diameter (d_p in Fig. 1e) which was constant throughout this work.

The plots in Fig. 15 also illustrate a band of steady-state hypervelocity p/D_c values ($\Delta(p/D_c)$) which range from 0.4 to 1.0 over a corresponding range of projectile densities from 2.2 to $\sim$17 Mg/m^3. The anomalous "hump" in the plots of p/D_c versus u_o data in Fig. 15 is also observed to be dependent upon the projectile density as well, and increasing in magnitude (p/D_c) with increasing projectile density.

The reason for this anomalous hump or hump-shaped feature is related to projectile fragmentation or the fragmentation onset velocity. Grady and Kipp [20] have described a well-documented series of experiments to determine the fragmentation onset velocity for a number of metallic projectiles having different densities. This threshold velocity was usually above about 2 km/s, and just sufficient to fragment the projectile. Livingstone *et al.* [21] have also recently used numerical simulations to predict the fragmentation onset velocity. The implications for the present experiments, especially implicit

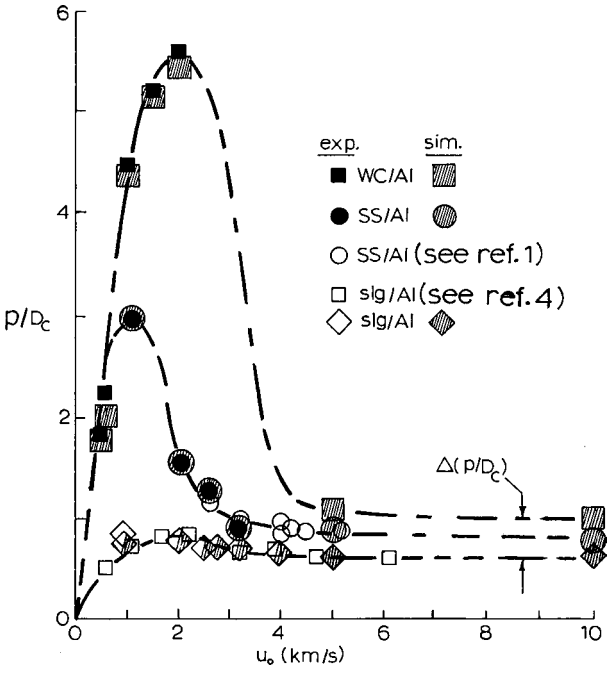

Figure 15 Experimental and computer simulated plots for p/D_c versus impact velocity (u_o) for the various projectile/target systems analyzed in this study. The data from Baker [1] is included as indicated. Prior data from Valerio *et al.* [4] is included as indicated.

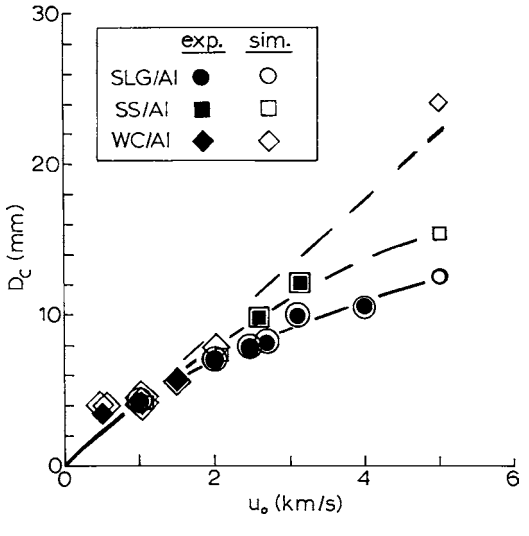

Figure 16 Experimental and simulated plots for D_c versus u_o for the various projectile/target systems analyzed in this study (Table III).

in the plots of Fig. 15, are that projectiles which are intact or in the initial stages of fragmentation will produce exaggerated crater depths in contrast to the crater diameters, which essentially match the projectile size (d_p in Fig. 1e). Fragmentation will occur earlier for brittle and lower-density projectiles such as the soda-lime glass projectiles in this study than for the ductile, more dense stainless steel; and more dense WC projectiles [20]. Consequently this would also be an argument against the stainless steel projectile peak in Fig. 15 from shifting downward (to lower values of u_o). Correspondingly, this would be an argument to increase the peak for the WC projectiles in Fig. 15 since the density is much higher. In fact, the cross-section view in Figs 3d and 5b indicate only partial fragmentation of the WC projectile at 2 km/s. The stainless steel projectile, on the otherhand, is completely fragmented at 3.15 km/s impact velocity and Fig. 15 shows the corresponding impact crater to be well off the hump, and close to the steady-state or hypervelocity value of p/D_c.

As it turns out, there is very little research directed at the observations of projectile fragmentation and correlations of crater debris with fragmentation simulations over a range of impact velocities characterizing the fragmentation onset velocity regime. These kinds of studies would provide some important insight into the specific features of the hump-shaped plots shown in Fig. 15.

Finally, Fig. 17 illustrates a representation of the culmination of valid computer simulations which have taken into account both crater geometry and microstructure-related issues utilizing a constant projectile (impact) velocity of 2 km/s for each of the same size (3.175 mm diameter) SLG, SS, and WC projectiles impacting an aluminum target. In effect, the final crater geometry, or more specifically the range of geometries, is essentially representative of the range of crater types described by Baker [1] at various impact velocities. However Fig. 17 shows these crater types for a range of projectile densities at the same low impact velocity. An interesting feature to note is that there is a reduction in the projectile fragmentation in going from Fig. 17a to c; an indication that the fragmentation onset velocity is increasing with projectile density. Similar time sequences have also been simulated for the same system over a range of velocities, and these features are in fact illustrated by systematically perusing the simulations shown in Figs 8 to 13. Fig. 17 is also indicative of the very essence of computer simulations in that once considered valid, time and variations in crater geometry and the behavior of the projectile during the cratering process can be viewed and examined. Otherwise, there is only the residual crater which has evolved throughout the time sequence; as illustrated experimentally in Figs 1 to 3.

4. Summary and conclusions

Impact craters in a series of projectile/target systems—SLG/Al, SS/Al, and WC/Al—have been examined and compared in this research program to explore the effects of impact velocity and projectile density on crater formation. Of special interest was the examination of an anomalous hump in plots of crater depth/diameter ratios (p/D_c) versus impact velocity, u_o, which was observed between about 1 and 2 km/s, and whose amplitude (or values of p/D_c) increased with density; extending from 0.8 for SLG projectiles with $\rho_p = 2.2$ Mg/m^3 to roughly 5.5 for WC projectiles with $\rho_p \cong 17$ Mg/m^3. This hump is related to the fragmentation onset velocity which is usually >2 km/s and increases with increasing projectile density. Before projectile fragmentation the crater diameter is essentially the size of the projectile diameter while the depth of penetration is optimized. With fragmentation the crater depth is reduced and correspondingly the diameter increases.

Residual microhardness maps constructed from measurements on impact crater half-sections were correlated with target microstructures surrounding the

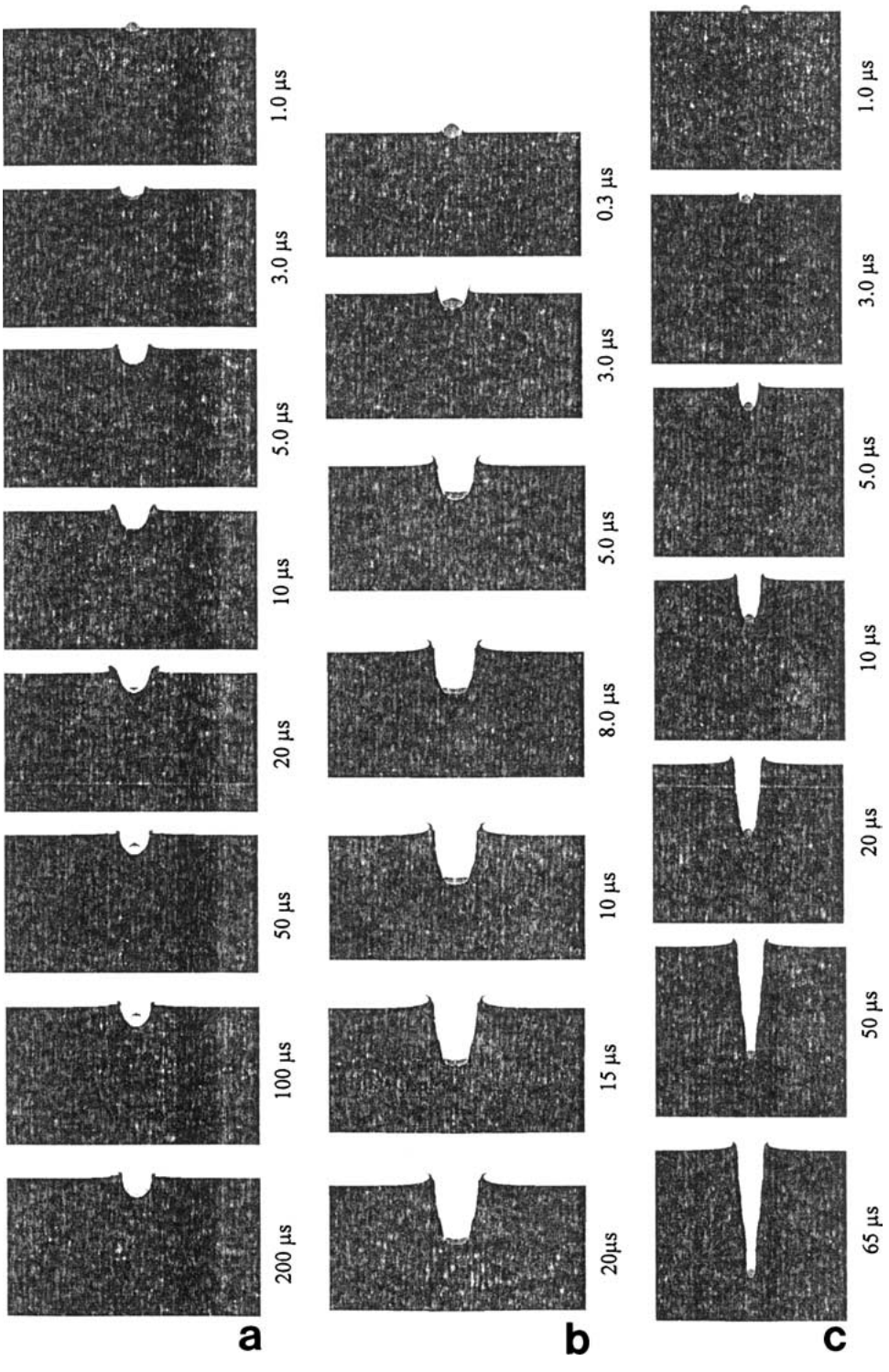

Figure 17 Computer simulations representing partial time sequences for impact crater formation by 3.175 mm diameter spherical projectiles impacting at 2 km/s. (a) Soda-lime glass projectiles. (b) Stainless steel projectiles. (c) Tungsten carbide projectiles. Times from impact are shown in μs.

impact craters. These microhardness profiles, along with the measured crater geometry parameters p, D_c and p/D_c as well as the crater shapes or types, were compared with 2-D impact crater computer simulations which also produced corresponding residual yield stress contour maps, which could be linearly related to the experimental microhardness maps by approximating the yield stress as one-third of the microhardness in equivalent units. By validating the computer simulations through matching crater shapes and corresponding residual yield stress—microhardness maps, crater simulations were extrapolated into the hypervelocity regime as an extension of the laboratory environment. These extrapolations illustrated the hypervelocity-steady-state values of p/D_c to be projectile density dependent at least to $u_o = 15$ km/s, and to vary from 0.6 to 1.0 for ρ_p between 2.2 and 17 Mg/m^3 respectively in contrast to the anomalous values of p/D_c at low impact velocity (1 to 2 km/s) of 0.8 to 5.5 as noted above. The simulations for impact velocities above 5 km/s indicated melting and solidification at the crater wall, and observations of craters in aluminum alloy structures on the NASA-LDEF satellite seemed to confirm this.

Acknowledgments

This research was supported by NASA MURED Grant NAG-9-1171 and NASA/Grant NAG-9-1100 through the NASA Johnson Space Center, Houston, TX. We are grateful to Dr. Fred Hörz at NASA Johnson for providing the impact experiments which made this study possible. The help of Dr. Chris Quan and Bence Gerber at Century Dynamics, Inc. in using the AUTODYN software is also gratefully acknowledged.

References

1. J. R. BAKER, *Int. J. Impact Engr.* **17** (1995) 25.
2. R. P. BERNHARD and F. HÖRZ, *ibid* **17** (1995) 69.
3. L. E. MURR, S. A. QUINONES, E. FERREYRA, T. A. AYALA, O. L. VALERIO, F. HÖRZ and R. P. BERNHARD, *Mater. Sci. Engr.* A **256** (1998) 166.
4. O. L. VALERIO, V. S. HERNANDEZ, S. A. QUINONES, L. E. MURR and F. HÖRZ, in "Fundamental Issues and Applications of Shock-Wave and High-Strain-Rate Phenomena", edited by K. P. Staudhammer, L. E. Murr and M. A. Meyers (Elsevier Science Ltd., Amsterdam, 2001) Chap. 49, p. 383.
5. H. A. ZOOK, *Lunar and Planetary Sci.* **21** (1990) 112.
6. L. E. MURR and W. H. KINARD, *Amer. Scient.* **81** (1993) 152.
7. J. A. M. McDONNEL (ed.), "Hypervelocity Impact in Space" (Univ. of Kent, Canterbury, U.K., 1992).
8. J. A. JOSELYN and E. C. WHIPPLE, *Amer. Scient.* **78** (1990) 126.
9. N. McBRIDE, S. F. GREEN and J.A. McDONNEL, *Adv. Space Res.* **23**(1) (1999) 73.
10. S. A. QUINONES and L. E. MURR, *Phys. Stat. Sol. (a)* **166** (1998) 763.
11. N. K. BIRNBAUM, M. COWLER, M. ITOH, M. KATAYAMA and H. OBATA, AUTODYN-An Interactive, Nonlinear Dynamic Analysis Program for Microcomputers Through Supercomputers, 9th Int. Conf. on Structural Mechanics in Reactive Technology, Lausanne, August, 1987.
12. C. T. HAYHURST, H. J. RANSON, D. J. GARDNER and N. K. BIRNBAUM, *Int. J. Impact Engr.* **17** (1995) 375.
13. G. R. JOHNSON and W. H. COOK, A. Constitutive Model and Data for Metals Subjected to Large Strains, High Strain Rates, and Temperatures, in Proc. 7th Int. Symposium on Ballistics, The Hague, 1983.
14. E. A. TAYLOR, K. T. SEMBELLS, C. J. HAYHURST, L. KAY and M. J. BURCHELL, *Int. J. Impact Engr.* **23** (1999) 895.
15. M. A. MEYERS, "Dynamic Behavior of Materials" (Wiley, NY, 1994).
16. M. H. RICE, R. G. McQUEEN and J. M. WALSH, *Solid State Phys.* **6** (1958) 1.
17. R. G. McQUEEN, S. P. MARSH, J. W. TAYLOR, J. N. FRITZ and W. J. CARTER, in "The Equation of State of Solids from Shock Wave Studies, High Velocity Impact Phenomena", edited by R. Kinslow (Academic Press, NY, 1970) p. 230.
18. T. H. SEE, M. K. ALLBROOKS, D. R. ATKINSON, C. R. SIMON and M. E. ZOLENSKY, Meteroid and Debris Impact Features Documented on The Long Duration Exposure Facility, NASA-JSC Report No. 24608, 1990.
19. L. E. MURR, C.-S. NIOU, S. A. QUINONES and K. S. MURR, *Scripta Metall. et Mater.* **27** (1992) 101.
20. D. E. GRADY and M. E. KIPP, Impact Failure and Fragmentation Properties of Metals, Sandia Report SAND98-0387 Sandia National Laboratories, Albuquerque, New Mexico, March, 1998.
21. J. H. G. LIVINGSTONE, K. VEROLME and C. J. HAYHURST, *Int. J. Impact Engr.* **26** (2001) 453.

Received 4 June 2003
and accepted 28 May 2004